ADVANCED MATERIALS INTERFACES
www.advmatinterfaces.de

Ambipolar Plasmon-Enhanced Photodetector Built on Germanium Nanodots Array/Graphene Hybrid

Min Gao, Ziao Tian, Shiwei Tang, Xiaowen Han, Miao Zhang, Zhongying Xue, Wei Zhu, Yongfeng Mei, Paul K. Chu, Gang Wang, and Zengfeng Di**

Graphene with gate-tunable electronic properties is promising as the channel materials in ambipolar multifunctional photodetectors. However, owing to the zero bandgap and weak light absorption, photodetectors fabricated on pristine graphene have low photoresponsivity. Herein, an ambipolar multifunctional photodetector with improved photocurrent and response speed is constructed on germanium (Ge) nanodots array-decorated graphene. The photocurrent map and simulated electric field distributions reveal that the enhanced photo-response is attributed to the localized surface plasmonic resonance effects by trapping light around the Ge nanodots. The photodetector exhibits ambipolar photo-response and the photocurrents can be tuned from negative to positive by applying different gate voltages due to the gate-tunable Fermi level of graphene. This ambipolar photodetector with fast response has excellent potential in imaging and sensing arrays as well as multifunctional photodetectors.

1. Introduction

Photodetectors are crucial to a myriad of applications including optical communication, military surveillance, and consumer electronics.[1] In particular ambipolar photodetectors that can switch between positive or negative photo-response depending on the external field[2,3] or illumination wavelength[4,5] provide the platform for multifunctional phototransistors with integrated circuit compatibilities such as light switching,[6–8] optical modulator,[9,10] and thermography.[11] However, common ambipolar materials like organic semiconductors cannot be synthesized precisely due to the unknown relationship between the molecular structure and system performance.[12] Graphene is a natural ambipolar material and its carrier polarity can be easily tuned by applying different gate voltages. In addition, on account of the atomic thickness and excellent electronic properties, graphene attracts much attention as promising channel materials in ambipolar photodetectors.[7,13] However, its gapless band feature and low light absorption (only 2.3%) spanning the visible to infrared regimes (IR) regimes result in low responsivity and detectivity of graphene-based photodetectors, consequently hampering the application of graphene to photo-detection.[14,15] Several heterostructures such as lateral graphene p-n junctions,[16] graphene-silicon Schottky junctions,[17,18] and graphene-MoS_2 hybrid[19] have been shown to have photo-detection properties but the complex fabrication process limits mass production of graphene-based photodetectors with high-performance.

In this work, Ge nanodots array is integrated with graphene to construct a plasmon-enhanced photodetector that capitalizes on the localized surface plasmonic resonance (LSPR) effects in which plasmons oscillate with conduction electrons and confine light in nanoscale volumes with enhanced electric field. Owing to the LSPR, light scattered by an individual nanodot can be easily collected by neighboring nanodots[20–22] to increase the photocurrent and shorten the response time (18.7 μs). In particular, as the carrier density and polarity of graphene can be easily tuned by the gate voltage, the photocurrent can be switched from negative to positive and therefore, the photodetector can be operated in the ambipolar mode. This ambipolar photodetector composed of the Ge nanodots array/graphene hybrid provides a convenient and valid strategy for mass production of high-performance photodetectors.

Dr. M. Gao, Prof. Z. Tian, Dr. X. Han, Prof. M. Zhang, Prof. Z. Xue, Prof. Z. Di
State Key Laboratory of Functional Materials for Informatics
Shanghai Institute of Microsystem and Information Technology
Chinese Academy of Sciences
Shanghai 200050, P. R. China
E-mail: zfdi@mail.sim.ac.cn

Dr. M. Gao, Dr. X. Han
Center of Materials Science and Optoelectronics Engineering
University of Chinese Academy of Sciences
Beijing 100049, P. R. China

Prof. S. Tang, Dr. W. Zhu, Dr. G. Wang
Department of Microelectronic Science and Engineering
School of Physical Science and Technology
Ningbo University
Ningbo 315211, P. R. China
E-mail: gangwang@nbu.edu.cn

Prof. Y. Mei
Department of Materials Science
Fudan University
Shanghai 200433, P. R. China

Prof. P. K. Chu
Department of Physics
Department of Materials Science and Engineering
and Department of Biomedical Engineering
City University of Hong Kong
Tat Chee Avenue, Kowloon, Hong Kong 999077, P. R. China

The ORCID identification number(s) for the author(s) of this article can be found under https://doi.org/10.1002/admi.202001122.

DOI: 10.1002/admi.202001122

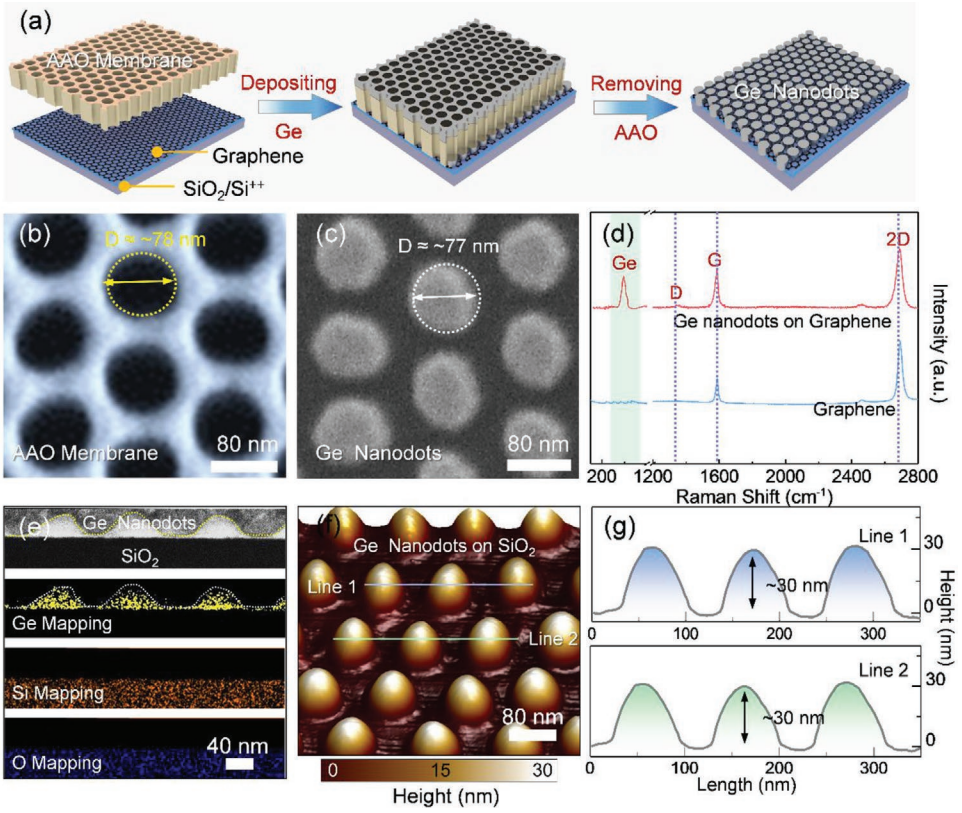

Figure 1. a) Schematic diagrams showing the synthesis of the Ge nanodots array on the graphene/SiO_2/Si substrate. b) SEM image of the AAO membrane (Scale bar = 80 nm. c) SEM image of the Ge nanodots array on the graphene/SiO_2/Si substrate (Scale bar = 80 nm). d) Raman spectra of Ge nanodots array/graphene/SiO_2/Si (red line) and graphene/SiO_2/Si (blue line). e) TEM image of the cross-sectional 30 nm thick Ge nanodots array/graphene/SiO_2/Si and corresponding TEM-EDS maps of Ge (yellow), Si (orange), and O (blue) (Scale bar = 40 nm). f) 3D AFM image of the Ge nanodots array/graphene/SiO_2/Si (Scale bar = 80 nm). g) Depth profile along Line 1 and Line 2 in panel f.

2. Results and Discussion

The anodic aluminum oxide (AAO) membrane is often used as a template to synthesize large-scale ordered arrays of nanostructures.[23,24] In our study, the geometry of the Ge nanodots array is defined by the selected AAO membrane as shown in **Figure 1**a. The AAO membrane is first transferred onto the graphene/SiO_2/Si substrate. According to the statistical analysis (Figure S1a–c, Supporting Information), the average diameter and periodicity of the AAO membrane are about 78 and 97 nm, respectively, which are verified by the zoom-in scanning electron microscopy (SEM) image in Figure 1b. Subsequently, a 30 nm thick Ge layer is deposited by thermal evaporation and then the AAO membrane is removed to yield a highly ordered Ge nanodots array on the graphene/SiO_2/Si substrate as revealed by Figure 1c and Figure S2, Supporting Information. Statistical analysis discloses that the average diameter of the Ge nanodots is 77 nm and the average periodicity is 96 nm (Figure S1d–f, Supporting Information) is consistent with the dimensions of the AAO membrane template. The presence of graphene is confirmed by comparing the Raman spectra collected from the graphene/SiO_2/Si and Ge nanodots array/graphene/SiO_2/Si. The characteristic features of graphene including the G band peak at 1580 cm^{-1} and the 2D band peak at 2700 cm^{-1} are shown in Figure 1d. Before deposition of the Ge nanodots array, graphene retains the high crystallinity after transferring to the SiO_2/Si substrate, as suggested by the absence of the D band at 1350 cm^{-1} and large I_{2D}/I_G ratio of 1.45 (Figure S3, Supporting Information). After deposition of the Ge nanodots array, the graphene signals change barely implying that the deposition process has little influence on the crystalline quality of graphene and the Ge nanodots array is responsible for the extra peak at 300 cm^{-1}. Figure 1e shows the cross-sectional transmission electron microscopy (TEM) image of the Ge nanodots array disclosing a uniform height of 30 nm, and the corresponding TEM-energy dispersive X-ray spectroscopy (TEM-EDS) images reveal that the Ge nanodots are disconnected from each other. Inheriting the regularity of the AAO membrane template, the Ge nanodots are well ordered forming an array pattern as shown by the 3D atomic force microscopy (AFM) image (Figure 1f). The line profiles of the Ge nanodots array (Figure 1g) show that the Ge nanodots have a periodicity of 100 nm, a uniform height of 30 nm, and an average diameter of 80 nm in agreement with the statistical analysis of the SEM image (Figure S1d–f, Supporting Information).

To evaluate the photoelectric conversion performance of Ge nanodots array/graphene, a standard device (**Figure 2**a) is fabricated and assessed using the semiconductor characterization system. Figure 2b displays the photo-response of the device illuminated with 1550 nm light at $V_{BG} = 0$ V and $V_{DS} = 1$ V with

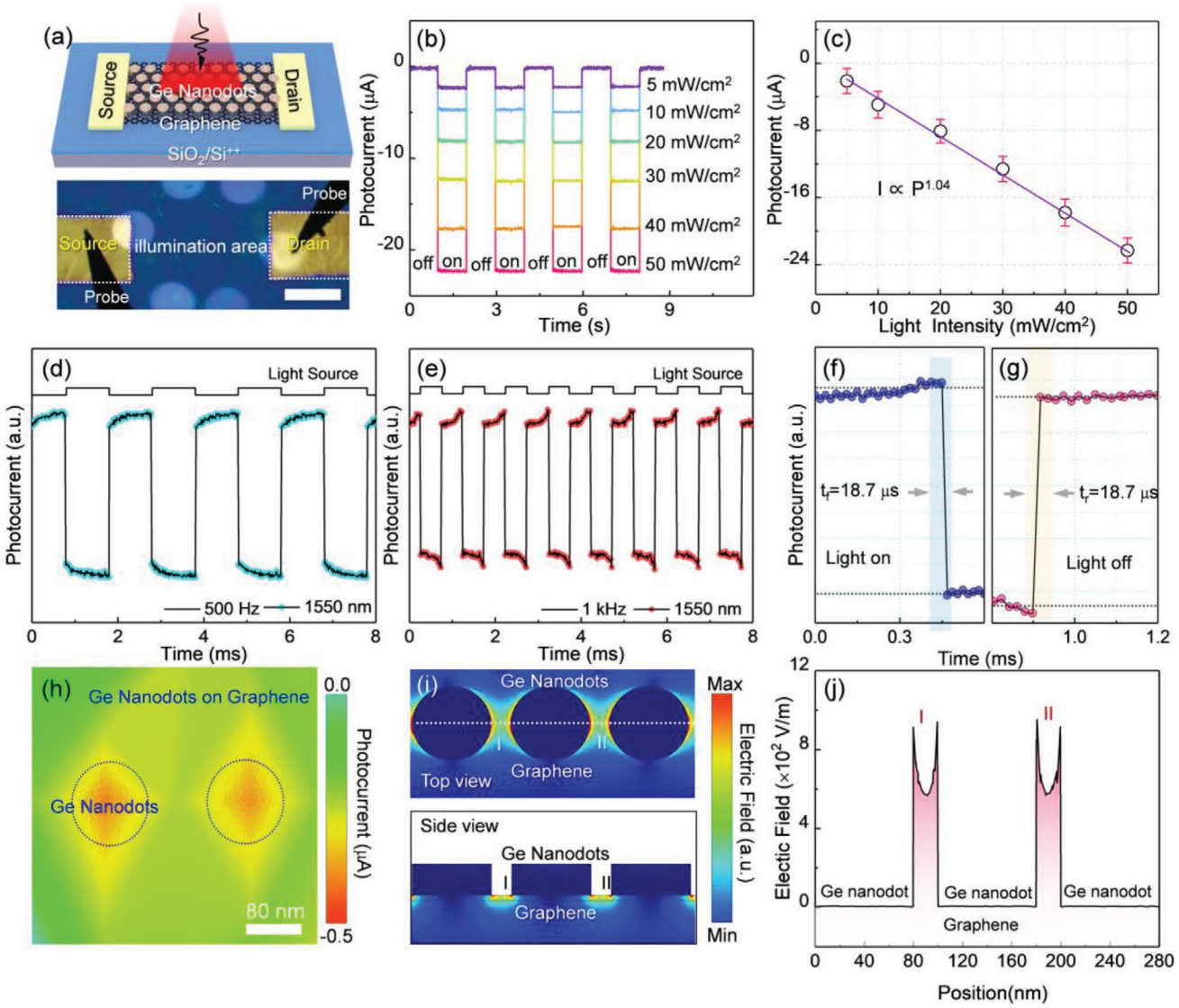

Figure 2. a) Top panel: Schematic of the Ge nanodots array/graphene/SiO_2/Si photodetector; Bottom panel: Optical image of the photodetector during measurement (Scale bar = 100 μm). b) Photo-response under the 1550 nm light illumination with different light intensities (V_{DS} = 1 V and V_{BG} = 0 V). c) Photocurrents of the photodetector versus light intensity with the red line being the fitted curve expressed as $I \propto P^{1.04}$. d,e) Photo-response under 1550 nm light illumination for frequencies of 500 Hz and 1 kHz. f,g) Fall time (t_f) and rise time (t_r) derived from the enlarged photo-response in panel (e). h) Photocurrent map under 1550 nm light illumination for an intensity of 1 mW cm^{-2} (Scale bar = 80 nm). The dashed circles represent the Ge nanodots. i) Plane view (top) and side view (bottom) of the simulated electric field distribution of the Ge nanodots on graphene under 1550 nm illumination. j) Electric field profile along the dotted line in panel i.

different light intensities. The photocurrent which exhibits excellent stability and reproducibility falls immediately in the on-state (under illumination) and rises in the off-state (without illumination) indicating a negative response. The photocurrent increases gradually as the light density goes up, from 5 up to 50 mW cm^{-2}, and it follows $I \propto P^{\theta}$, where θ determines the responsivity[25] (Figure 2c). Data fitting yields a θ value of about 1.04 suggesting a low density of trap centers in the Ge nanodots array/graphene photodetector.[26] The responsivity (R), specific detectivity (D), and noise equivalent power (NEP) are often used to evaluate the performance of a photodetector and are calculated by the following equations:[18,25]

$$R = \frac{I_P}{P_{in}} \tag{1}$$

$$D = \frac{A^{1/2}R}{(2qI_D)^{1/2}} \tag{2}$$

$$NEP = \frac{\sqrt{A}}{D} \tag{3}$$

where I_P, P_{in}, A, and I_D are the photocurrent, effective light power, device area, and dark current, respectively. For the Ge nanodots array/graphene photodetector, R, D, and NEP

Table 1. Comparison of the performance of graphene-based photodetectors.

Device architecture	Rise time (t_r)	Fall time (t_f)	Responsivity [mAW^{-1}]	Detectivity [cm Hz$^{1/2}$ W^{-1}]	Ref.
Ge nanodots/graphene	18.7 µs	18.7 µs	44.5	2.16×10^{10}	Our work
Graphene–Ge Schottky junction	23 µs	108 µs	51.8	1.38×10^{10}	[26]
PbS quantum dots/graphene	10 ms	10 ms	1×10^{10}	7×10^{13}	[25]
PbS quantum dots/N,S co-doped graphene	3 ms	200 ms	2.6×10^{7}	5.5×10^{12}	[27]
$CsPbBr_{3-x}I_x$ perovskite nanocrystals/graphene	0.81 s	3.65 s	8.2×10^{11}	2.4×10^{16}	[28]
$CsPbCl_3$ perovskite nanocrystals/graphene	0.3 s	0.35 s	$>10^9$	$>10^{13}$	[29]
$WO_{2.9}$/graphene	36 µs	35 µs	824	–	[30]
$Cu_{3-x}P$ colloidal nanocrystals/graphene	420 ms	1 s	934	5.98×10^{12}	[31]
Graphene on InGaN quantum dots	>100 s	>100 s	$>10^9$	5.8×10^{14}	[32]

are estimated to be 45 mA W^{-1}, 2.16×10^{10} cm Hz$^{1/2}$ W^{-1}, and 4.9 nW Hz$^{1/2}$, respectively, when the light intensity is 50 mW cm^{-2}. Moreover, the photodetector also has good performance in the visible light range (with light wavelengths of 440 and 780 nm) as shown in Figure S4, Supporting Information. In addition, the photodetector exhibits reliable response and operates very well upon 1550 nm illumination even at high frequencies of 500 Hz (Figure 2d) and 1 kHz (Figure 2e). The response time (current fall time, t_f) and recovery time (current rise time, t_r) are 18.7 and 18.7 µs, respectively, as shown in Figure 2f,g. The photodetector shows faster response than other graphene-based photodetectors reported previously (**Table 1**).

The high-resolution photocurrent image in Figure 2h shows two enhanced spots around two individual Ge nanodots separated by a distance consistent with the periodicity of the Ge nanodots array. To further explore the enhancement effects, finite element method (FEM) simulation is conducted. Figure 2i shows the plane view and cross-sectional view of the simulated electric field distribution during 1550 nm light illumination. It clearly shows an enhanced electric field in the proximity of the Ge nanodots (Figure 2j) which can be ascribed to the LSPR effect in which the incident light is absorbed and scattered by the Ge nanodots leading to the enhanced oscillation and local electric field. More important, the enhanced electric field can greatly facilitate the separation process of photo-generated hole-electron pairs in the Ge nanodots and the transfer process of photo-generated holes to graphene, which consequently increase the response as previously observed from Au nanoarrays/MoS_2[20] and $WO_{2.9}$ nanoarrays/graphene.[30] The performance of Ge nanodots array/graphene photodetector closely correlates with the distribution and the diameter of Ge nanodots (Figures S5 and S6, Supporting Information).

To elucidate the mechanism for the negative photo-response of the Ge nanodots array/graphene photodetector, photocurrent curves are collected at different back-gate voltages as shown in **Figure 3**a. When $V_{BG} > -3$ V, the photocurrent is negative but the photocurrent changes to positive when $V_{BG} < -3$V. It suggests that the Ge nanodots array/graphene photodetector is an ambipolar one in which the sign of the photocurrent can be easily switched by applying different gate voltages. This unique

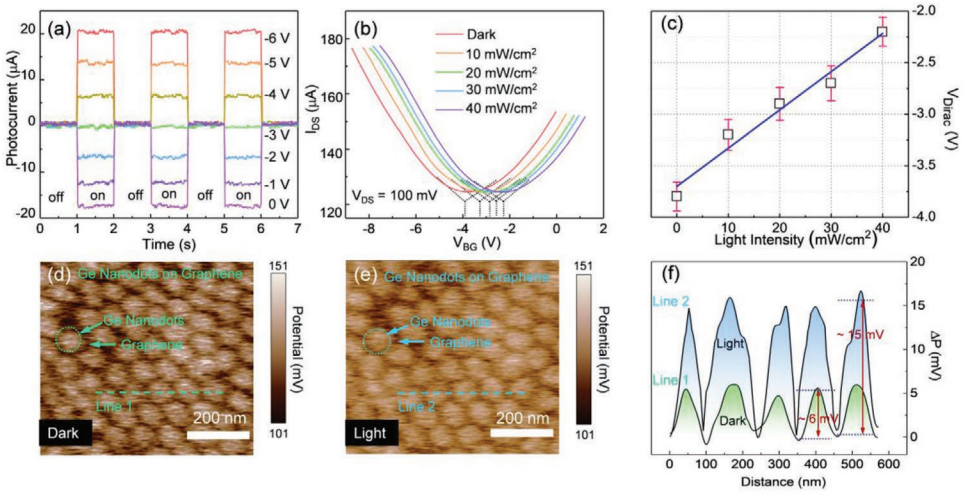

Figure 3. a) Photo-response of the Ge nanodots array/graphene photodetector device under 1550 nm illumination for different back-gate voltages from $V_{BG} = 0$ V to $V_{BG} = -6$ V in −1 V steps. The source-drain bias is 1 V and light intensity is 40 mW cm^{-2}. b) Transfer characteristics under 1550 nm illumination for different light intensities. c) Relationship between V_{Dirac} and light intensity. SKPM images of the Ge nanodots array/graphene d) in dark and e) in light irradiation. The scale bar is 80 nm. f) Surface potential profiles in the dark (green line 1 in panel (d)) and upon light illumination (blue line 2 in panel (e)).

ambipolar property has resemblance to the gate-tunable carrier species of graphene.[4] To validate the ambipolar behavior, the transfer characteristics are determined during exposure to light of different intensity (Figure 3b). The I_{DS}–V_{BG} curve of pristine graphene in Figure S7, Supporting Information, shows the typical gate-tunable characteristic with the Dirac point at 12.5 V indicative of the p-type behavior as a result of additional oxidation or surface absorption.[28] After depositing Ge nanodots on graphene, the Dirac point shifts negatively to −3.8 V implying that electrons are transferred from the Ge nanodots to graphene. As the light intensity is increased from 0 to 40 mW cm^{-2}, the Dirac point shifts from −3.8 V to ≈−2.2 V as shown in Figure 3c. The shift in the Dirac point suggests an enhanced hole-transfer effect from Ge nanodots to graphene with increasing light intensity. In general, the photodetector produces a negative photocurrent, that is, $I_{dark} > I_{light}$ when $V_{BG} > V_{Dirac}$, but the photocurrent changes to positive, that is, $I_{dark} < I_{light}$ when $V_{BG} < V_{Dirac}$. It is verified by the photodetection behavior of the photodetector under illumination by a large light intensity of 40 mW cm^{-2} as shown in Figure 3a.

Scanning Kelvin probe microscopy (SKPM) is an effective method to explore the flow of the separated electrons and holes by measuring the surface potential difference (SPD) between graphene and Ge nanodots without and with light irradiation.[33–36] SPD is defined by the difference in the Fermi level between graphene and Ge nanodots as shown in the following:

$$\Delta E_f = \Phi_{graphene} - \Phi_{Ge} = eP_{Ge} - eP_{graphene} = e\Delta P \quad (4)$$

where $\Phi_{graphene}$, $P_{graphene}$, and Φ_{Ge}, P_{Ge} correspond to the work function and surface potential of graphene and Ge nanodots, respectively. As shown in the SKPM images (Figure 3d,e), the SPD of the Ge nanodots/graphene hybrid is obviously higher when exposed to light. The detailed SPD analysis is shown in Figure S8, Supporting Information, in which $P_{graphene}$, P_{Ge}, and ΔP are well defined. Figure 3f shows the corresponding ΔP profiles along the lines in Figure 3d,e yielding an average $\Delta E_f = e\Delta P = 6$ meV at dark and $\Delta E_f = 15$ meV with light. The larger SPD upon light irradiation confirms the transfer of holes from the Ge nanodots to graphene, which is in agreement with the transfer characteristics in Figure 3b,c.

The energy band models are established to understand the flow of electrons and holes in the Ge nanodots array/graphene system. Prior to the deposition of Ge nanodots, the Fermi level of graphene is lower than that of Ge nanodots as shown in **Figure 4**a. After deposition of Ge nanodots on graphene, electrons are transferred from Ge nanodots to graphene to equilibrate the Fermi level between Ge and graphene consequently inducing electron doping in graphene and the shift

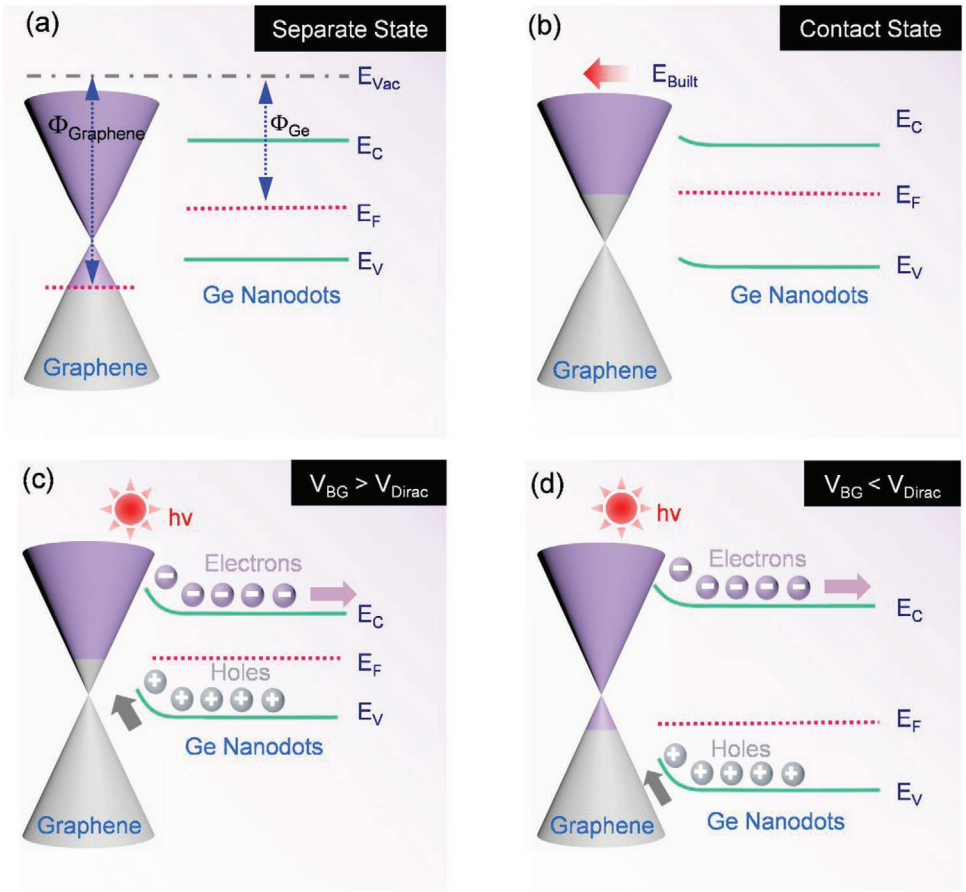

Figure 4. a,b) Energy band diagrams of the Ge nanodots array/graphene system in the separate state and contact state. c,d) Energy band diagrams of the Ge nanodots array/graphene system in the contact state under illumination for $V_{BG} > V_{Dirac}$ and $V_{BG} < V_{Dirac}$, respectively.

of Dirac point to a negative value. Therefore, the valence band and conduction band of Ge bend upward to the interface creating a built-in field (Figure 4b) .[28] Figure 4c,d show the energy band models for $V_{BG} > V_{Dirac}$ and $V_{BG} < V_{Dirac}$, respectively. The SKPM is measured at zero bias corresponding to the $V_{BG} > V_{Dirac}$ case. In this case, when exposed to 1550 nm illumination, the photo-generated hole-electron pairs in the Ge nanodots are separated by the built-in electric field and holes are transferred to graphene as a doping effect while electrons are trapped in the Ge nanodots. Since graphene is electron-dominated at $V_{BG} > V_{Dirac}$, the transferred photo-generated holes recombine with electrons to decrease the Fermi level of graphene and increase SPD under light illumination and the negative photocurrent. As for the $V_{BG} < V_{Dirac}$ case (Figure 4d), graphene is hole-dominated, and the photo-generated holes from the Ge nanodots increase the density of holes in graphene to increase the current and produce a positive photocurrent.[37] Therefore, the photocurrent of the Ge nanodots array/graphene photodetecting system is extremely sensitive to the gate bias and the photocurrent can be tuned from negative to positive when the gate voltage crosses the Dirac point, which is essential for the design of a high-performance ambipolar photodetector.

3. Conclusion

A high-performance ambipolar photodetector is constructed with Ge nanodots array-decorated defect-free graphene. The periodic Ge nanodots increase the local electric field near the graphene layer due to the LSPR effect giving rise to fast response and recovery. In addition, owing to the gate-tunable carrier polarity and density of graphene, the photocurrent can be tuned from negative to positive as the gate bias is varied near the Dirac point of graphene thus behaving as an ambipolar photodetector. Our work reveals a convenient approach to design and produce high-performance photodetectors by integrating 2D materials with plasmonic nanostructures.

4. Experimental Section

AAO Membrane Transfer: The polymethyl methacrylate (PMMA)/AAO membrane (purchased from TopMembranes Technology) with an initial pore size of 78 nm and periodicity of 97 nm was placed in an acetone bath for 30 min to dissolve the PMMA layer; and the residual AAO membrane was then picked up by the graphene/300 nm SiO_2/Si substrate (purchased from SixCarbon Technology Shenzhen).

Photodetector Fabrication: The source and drain electrodes defined by standard photolithography were formed on the monolayer graphene/300 nm SiO_2/Si and Ti/Au (10 nm/100 nm) was deposited by thermal evaporation. Afterward, the graphene channel was patterned by another photolithographic process and etched by an inductively coupled plasma. The AAO membrane was transferred to the graphene channel and a 30 nm thick Ge film was directly deposited onto the AAO/graphene film by thermal evaporation with the evaporation rate of 0.1 nm s^{-1}. After removing the AAO membrane by a tap, the device was annealed at 280 °C for 5 h under a mixture of H_2 and Ar (10:1 sccm flow rates) to remove the adsorbate and contaminants.

Photodetector Characterization: The photocurrent was measured on an Agilent (B1500A) semiconductor parameter analyzer together with the Keithley 2400 semiconductor characterization system. The power-tunable laser with a wavelength of 1550 nm was employed under ambient conditions and the on and off periods were controlled by a mechanical shutter.

FEM Simulation: The electric field of the Ge nanodots array/graphene system upon illumination with a 1550 nm light source was simulated by FEM. The structure consisting of the Ge nanodots array (periodicity of 96 nm, diameter of 77 nm, and height of 30 nm), monolayer graphene, 300 nm SiO_2, and a semi-infinite Si layer was adopted in the simulation.

Supporting Information

Supporting Information is available from the Wiley Online Library or from the author.

Acknowledgements

The authors thank Key Research Project of Frontier Science, Chinese Academy of Sciences (QYZDB-SSW-JSC021), National Science and Technology Major Project (2016ZX02301003), National Natural Science Foundation of China (Grant No. 51925208, 61974157, 61851401, and 11704204), Strategic Priority Research Program (B) of the Chinese Academy of Sciences (XDB30030000), Science and Technology Commission of Shanghai Municipality (19JC1415500), City University of Hong Kong Strategic Research Grant (SRG) Nos. 7005264 and 7005105.

Conflict of Interest

The authors declare no conflict of interest.

Keywords

ambipolar photodetectors, Ge nanodots, graphenes, plasmonic resonances

Received: June 23, 2020
Revised: July 23, 2020
Published online:

[1] J. H. Li, L. Y. Niu, Z. J. Zheng, F. Yan, *Adv. Mater.* **2014**, *26*, 5239.
[2] T. Wakahara, P. D'Angelo, K. Miyazawa, Y. Nemoto, O. Ito, N. Tanigaki, D. D. C. Bradley, T. D. Anthopoulos, *J. Am. Chem. Soc.* **2012**, *134*, 7204.
[3] J. J. Wang, F. Wang, Z. X. Wang, R. Q. Cheng, L. Yin, Y. Wen, Y. Zhang, N. N. Li, X. Y. Zhan, X. H. Xiao, L. P. Feng, J. He, *Adv. Sci.* **2019**, *6*, 1801841.
[4] J. Yoo, J. Pyo, J. H. Je, *Nanoscale* **2014**, *6*, 3557.
[5] W. Y. Liu, J. S. Lee, D. V. Talapin, *J. Am. Chem. Soc.* **2013**, *135*, 1349.
[6] W. T. Huang, Y. H. Lin, T. D. Anthopoulos, *ACS Appl. Mater. Interfaces* **2018**, *10*, 10202.
[7] A. K. Geim, K. S. Novoselov, *Nat. Mater.* **2007**, *6*, 183.
[8] T. D. Anthopoulos, *Appl. Phys. Lett.* **2007**, *91*, 113513.
[9] M. Liu, X. B. Yin, E. Ulin-Avila, B. S. Geng, T. Zentgraf, L. Ju, F. Wang, X. Zhang, *Nature* **2011**, *474*, 64.
[10] X. Hu, J. Wang, *Nanophotonics* **2018**, *7*, 651.
[11] P. K. Herring, A. L. Hsu, N. M. Gabor, Y. C. Shin, J. Kong, T. Palacios, P. Jarillo-Herrero, *Nano Lett.* **2014**, *14*, 901.
[12] X. T. Zhang, H. L. Dong, W. P. Hu, *Adv. Mater.* **2018**, *30*, 1801048.
[13] S. Das Sarma, S. Adam, E. H. Hwang, E. Rossi, *Rev. Mod. Phys.* **2011**, *83*, 407.

[14] Y. B. Zhang, T. T. Tang, C. Girit, Z. Hao, M. C. Martin, A. Zettl, M. F. Crommie, Y. R. Shen, F. Wang, *Nature* **2009**, *459*, 820.
[15] G. Wang, M. Zhang, Y. Zhu, G. Q. Ding, D. Jiang, Q. L. Guo, S. Liu, X. M. Xie, P. K. Chu, Z. F. Di, X. Wang, *Sci. Rep.* **2013**, *3*, 2465.
[16] G. Wang, M. Zhang, D. Chen, Q. L. Guo, X. F. Feng, T. C. Niu, X. S. Liu, A. Li, J. W. Lai, D. Sun, Z. M. Liao, Y. Q. Wang, P. K. Chu, G. Q. Ding, X. M. Xie, Z. F. Di, X. Wang, *Nat. Commun.* **2018**, *9*, 5168.
[17] K. E. Chang, T. J. Yoo, C. Kim, Y. J. Kim, S. K. Lee, S. Y. Kim, S. Heo, M. G. Kwon, B. H. Lee, *Small* **2018**, *14*, 1801182.
[18] X. M. Li, M. Zhu, M. D. Du, Z. Lv, L. Zhang, Y. C. Li, Y. Yang, T. T. Yang, X. Li, K. L. Wang, H. W. Zhu, Y. Fang, *Small* **2016**, *12*, 595.
[19] H. Xu, J. X. Wu, Q. L. Feng, N. N. Mao, C. M. Wang, J. Zhang, *Small* **2014**, *10*, 2300.
[20] J. S. Miao, W. D. Hu, Y. L. Jing, W. J. Luo, L. Liao, A. L. Pan, S. W. Wu, J. X. Cheng, X. S. Chen, W. Lu, *Small* **2015**, *11*, 2392.
[21] Z. Y. Ni, L. L. Ma, S. C. Du, Y. Xu, M. Yuan, H. H. Fang, Z. Wang, M. S. Xu, D. S. Li, J. Y. Yang, W. D. Hu, X. D. Pi, D. R. Yang, *ACS Nano* **2017**, *11*, 9854.
[22] D. Y. Guo, C. X. Shan, K. K. Liu, Q. Lou, D. Z. Shen, *Nanoscale* **2015**, *7*, 18908.
[23] C. Mijangos, R. Hernandez, J. Martin, *Prog. Polym. Sci.* **2016**, *54-55*, 148.
[24] L. Y. Wen, Z. J. Wang, Y. Mi, R. Xu, S. H. Yu, Y. Lei, *Small* **2015**, *11*, 3408.
[25] G. Konstantatos, M. Badioli, L. Gaudreau, J. Osmond, M. Bernechea, F. P. G. de Arquer, F. Gatti, F. H. L. Koppens, *Nat. Nanotechnol.* **2012**, *7*, 363.
[26] L. H. Zeng, M. Z. Wang, H. Hu, B. Nie, Y. Q. Yu, C. Y. Wu, L. Wang, J. G. Hu, C. Xie, F. X. Liang, L. B. Luo, *ACS Appl. Mater. Interfaces* **2013**, *5*, 9362.
[27] L. Zheng, W. J. Zhou, Z. J. Ning, G. Wang, X. H. Cheng, W. D. Hu, W. Zhou, Z. D. Liu, S. W. Yang, K. M. Xu, M. Luo, Y. H. Yu, *Adv. Opt. Mater.* **2018**, *6*, 1800985.
[28] D. H. Kwak, D. H. Lim, H. S. Ra, P. Ramasamy, J. S. Lee, *RSC Adv.* **2016**, *6*, 65252.
[29] M. G. Gong, R. Sakidja, R. Goul, D. Ewing, M. Casper, A. Stramel, A. Elliot, J. Z. Wu, *ACS Nano* **2019**, *13*, 3714.
[30] Y. F. Yu, Y. Sun, Z. L. Hu, X. H. An, D. M. Zhou, H. Z. Zhou, W. H. Wang, K. Y. Liu, J. Jiang, D. D. Yang, Z. Zafar, H. B. Zeng, F. Q. Wang, H. M. Zhu, J. P. Lu, Z. H. Ni, *Adv. Mater.* **2019**, *31*, 1903829.
[31] T. Sun, Y. J. Wang, W. Z. Yu, Y. S. Wang, Z. G. Dai, Z. K. Liu, B. N. Shivananju, Y. P. Zhang, K. Fu, B. Shabbir, W. L. Ma, S. J. Li, Q. L. Bao, *Small* **2017**, *13*, 1701881.
[32] A. Q. Hu, H. J. Tian, Q. L. Liu, L. Wang, L. Wang, X. Y. He, Y. Luo, X. Guo, *Adv. Opt. Mater.* **2019**, *7*, 1801792.
[33] L. Su, Z. X. Zhao, H. Y. Li, J. Yuan, Z. L. Wang, G. Z. Cao, G. Zhu, *ACS Nano* **2015**, *9*, 11310.
[34] J. T. Lu, Z. Q. Zheng, J. D. Yao, W. Gao, Y. Zhao, Y. Xiao, J. B. Li, *Small* **2019**, *15*, 1904912.
[35] W. Kim, C. F. Li, F. A. Chaves, D. Jimenez, R. D. Rodriguez, J. Susoma, M. A. Fenner, H. Lipsanen, J. Riikonen, *Adv. Mater.* **2016**, *28*, 1845.
[36] R. Pearce, J. Eriksson, T. Iakimov, L. Hultman, A. L. Spetz, R. Yakimova, *ACS Nano* **2013**, *7*, 4647.
[37] K. Hu, F. Teng, L. X. Zheng, P. P. Yu, Z. M. Zhang, H. Y. Chen, X. S. Fang, *Laser Photonics Rev.* **2017**, *11*, 1600257.

